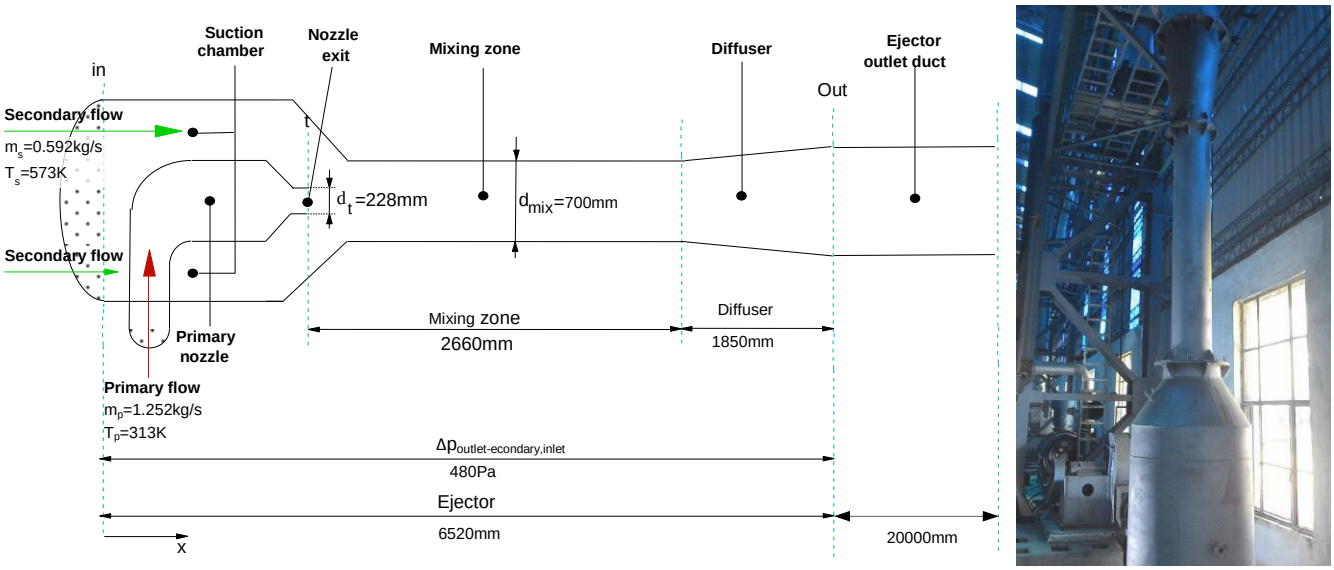

Figure 1 Ejector studied: layout (left) and photography of the system (right)

2.2. Ejector theory and modeling

Ejector is a device constituted by a primary nozzle, a suction chamber, a mixing zone and a diffuser. A high-pressure primary flow expands in the primary nozzle, entrains a secondary flow in the suction chamber, they mix and a diffuser compresses the mixed stream. The combined effects of entrainment, mixing and compression are the reasons why ejectors are studied for energy applications. Most of the existing ejector models are developed for refrigeration and SOFC application, where supersonic ejectors are used, and there are very few researches for subsonic ejectors. Unlike the refrigeration and the SOFC sectors in which the convergent–divergent ejector nozzle is widely used, the convergent nozzle is mostly prevalent in PEM Fuel Cell applications to avoid water condensation (due to low working temperature) in primary and secondary flow. In the present plant, a convergent nozzle is used; however, its geometry, working fluids and operating conditions are very different from the one of an ejector used in a PEM recirculation system [6, 7] . Therefore, the 1D models of the literature can not be used for evaluating its performance. Furthermore, a view of the internal flow behavior is necessary for a future optimization of the component and, in this framework, CFD modeling represents a useful tool [8].

3. CFD Model

3.1. Mesh

A 3D symmetric representation of the experimental ejector is used. The studies found in the literature generally consider 2D or 2D axi-symmetric computational domains [9]. Pianthong et al. [10], comparing a 2D and a 3D domain, found that the simplification is acceptable. Hemidi et al. [11, 12] stated that the 2D simplification is correct when ejector is operating at on-design condition, but the 2D simplification is not completely checked when ejector is operating at off-design condition. In the present case a 3D domain is chosen to (i) take into account of the effects of the curved pipe and (ii) take into account the effect of the change in geometry from the exhaust gas duct (square section) to ejector base (circular section) (Figure 2). It should not escape notice that the present geometry has some well-known issue for RANS simulations: (i) the change of geometry at inlet (from square duct to a circular section), (ii) the curved pipe and the (iii) diffuser inlet. The 3D discretization may help in the correct representation of the flow behavior. Indeed, a preliminary study a 2D domain discretization was attempted but lots of phenomena can not be captured. Due to the symmetric nature of the ejector, only half ejector was modeled. Criteria for the choice of the final mesh density were [13]: (i) the maximum skewness was below 6, (ii) the orthogonally was not less than 75 and (iii) The maximum growth rate from one element to the next was 20%. A grid independency study was conducted on three grids and 2.3 million elements composed the resulting grid. Further details on grid independency can be found in section 4.1. Grid elements are (i) tetrahedrons for the nozzle and suction chamber zone (refer to the zone 1 in Figure 2) and (ii) hexahedrons for the rest of the domain (zone 2). Mesh was refined on mixing layer and on proximity of the walls.

3.1. Governing equations

The steady state RANS equations for turbulent incompressible Newtonian fluid flow are used:

$$\frac{\partial U_i}{\partial x_i} = 0 \tag{1}$$

$$\frac{\partial \left(U_i U_j\right)}{\partial x_j} = -\frac{1}{\rho}\frac{\partial \overline{p}}{\partial x_i} + \frac{\partial}{\partial x_j}\left[\nu\left(\frac{\partial U_i}{\partial x_j} + \frac{\partial U_j}{\partial x_i} - \frac{2}{3}\frac{\partial U_l}{\partial x_l}\delta_{ij}\right)\right] + \frac{\partial}{\partial x_j}\left(-\overline{u_i' u_j'}\right) \tag{2}$$

$$c_p \frac{\partial \left(\overline{T} U_j\right)}{\partial x_j} = \frac{\kappa}{\rho}\frac{\partial^2 \overline{T}}{\partial x_i \partial x_j} + c_p \frac{\partial}{\partial x_j}\left(-\overline{u_j' T'}\right) \tag{3}$$

where the ensemble average is given here for the general quantities. The Reynolds averaged approach requires Reynolds stress components $\tau_{ij} = -\rho \overline{u_i' u_j'}$ and Reynolds-average scalar transport equation extra terms $-\overline{u_j' T'}$ to be modelled in an appropriate way.

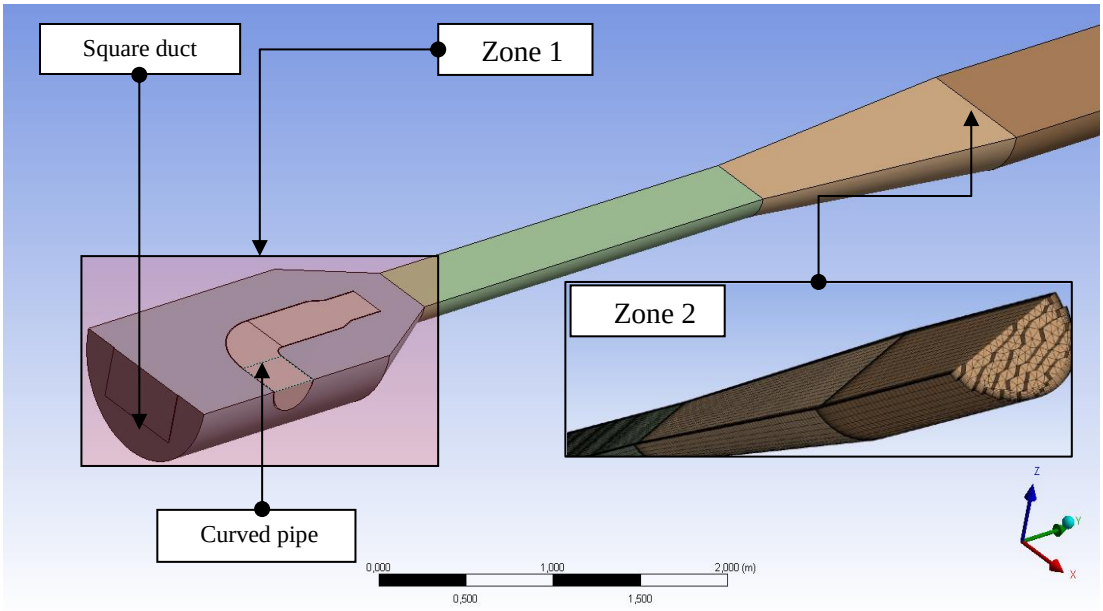

Figure 2 Ejector studied computational representation

3.2. **Solver**

The commercial software ANSYS-Fluent release 14.5.7, based on the finite volume approach, was used for solving the set of governing equations. The discretized equations, along with the initial and boundary conditions, were solved using the segregated solution method. The SIMPLE algorithm is employed for the pressure–velocity coupling. A second-order upwind discretization scheme was used for the energy equation, the momentum equation and the turbulent quantities.

3.3. **Turbulence modeling**

3.3.1. *Turbulence models*

The fluid flow in the ejector is turbulent. An evaluation of turbulence modeling is a mandatory step due to its large influence on the results. We have considered three turbulence models: the *k-ε* Realizable, the *k-ω* SST model and the RSM model. The performances of RANS turbulence models were evaluated accordingly to: (i) convergence capability and (ii) comparison with pressure experimental data. The RSM model experienced convergence problems and its results, except for the comment upon the convergence, have not been presented here. In the literature there are some studies concerning the comparison of RANS turbulence models for ejector. Bartosiewicz et al. [14] have compared the performance of six RANS turbulence models and the *k-ε* RNG and k-ω SST best predict the shock phase, strength, and the mean line of pressure recovery. Dvorak and Vit [15] compared different turbulence models using hot wire anemometry experimental results in terms of the static pressure at wall, velocity profile and turbulence intensity. They suggested *k-ε* Realizable as the most promising turbulence models. Kolar and Dvorak [16] verify the k–ω SST turbulence model by comparison with experimental Schlieren picture in terms of shock wave prediction and boundary layer separation. Gagan et al. [17] used a PIV technique for flow visualization and compared it with numerical results obtained for various turbulence models. They recommended the k–ε standard model. The k–ε Standard, k–ε Realizable and RSM models predict accurately the entrainment ratio. The k–ε RNG, RSM as well as k–ω do not predict vortex a region downstream nozzle. Besagni et al. [18] have suggested the *k-ω* SST as a promising turbulence model for convergent nozzle ejector, in terms of velocity and thermal field prediction. In this study, we have compared the *-ε* Realizable and the *k-ω* SST because of their good performances for ejector such as reported in the literature.

3.3.2. *Wall treatment*

The *k-ω* SST did not need a near wall treatment because its mathematical structure already emphasizes on the flow close to the wall. A non-equilibrium wall function has been used for the *k-ε* Realizable and the RSM. The use of a wall function in a computational flow solver allows fewer points to be placed near wall. This results in a better quality mesh, fewer number of computational point and a reduction in computing time.

3.4. **Boundary conditions**

Boundary conditions have been settled accordingly with the measurements: we have imposed the mass flow rate at the entrance of the primary flow ($m_{primary}$ = 1.252 kg/s) and the secondary flow ($m_{secondary}$ = 0.592 kg/s), whereas we have imposed the atmospheric pressure at the outlet. Temperature boundary conditions were settled as $T_{primary}$ = 313K and $T_{secondary}$ = 573 K for the primary and secondary flow, respectably. Wall conditions were set as adiabatic and no slip. Concerning the turbulent boundary conditions, hydraulic diameter and turbulence intensity I were chosen: $I_{primary}$ = 5% and for the $I_{secondary}$ = 3%.

3.5. **Working fluids**

The primary and secondary working fluids were air (MM = 28.97 kg/kmol, c_p = 1186.37 J/kgK, μ = $3.263 \cdot 10^{-5}$ kg s/m) and exhaust gases (MM = 27.68 kg/kmol, c_p = 1006.43 J/kgK, μ =$1.789 \cdot 10^{-5}$ kg s/m), respectively. Both the primary and the secondary flow are incompressible and their thermodynamic properties were evaluated at the inlet conditions. In order to simulate the mixing of the two streams we have employed a mixture approach.

3.6. **Convergence criteria**

The solution is considered as converged when all the following converging criteria are satisfied simultaneously: (i) numerical residuals decrease by six orders of magnitude; (ii) the normalized unbalance of mass flow rates had to be less than 10^{-7} (relative value); (iii) the area-weighed-averaged value for inlet pressure of primary and secondary flow is constant.

4. CFD model results

In this section, the CFD model results are critically outlined [19]. At first, the grid independency results are detailed. At second, the validation procedure is explained and the turbulence models are evaluated on the basis of convergence capability and accuracy. At last, the local flow behavior is investigated and the discrepancies between the turbulence models are here clarified.

4.1. **Grid independency**

Three different grids are analyzed: the coarse mesh is composed about by 1.1 million elements, the medium one is composed by 2.3 million elements and the fine one of about 3.4 million elements. The grid independency has been evaluated using both global and local data. The results presented refers to *k-ε* Realizable turbulence model. Concerning the global data, the difference between pressure outlet and the static pressure of secondary flow is compared: (i) $\Delta p_{coarse\text{-}mesh}$ = 734.1Pa, (ii) $\Delta p_{medium\text{-}mesh}$ = 550.3Pa and (iii) $\Delta p_{fine\text{-}mesh}$ = 551.5Pa. Concerning, the local data, axial velocity profiles are compared (Figure 3). In the suction and in the mixing zone there is higher discrepancy between the coarse and the other two grids, which on the other hand show a more similar trend. Therefore, the grid independency is reached for the medium mesh.

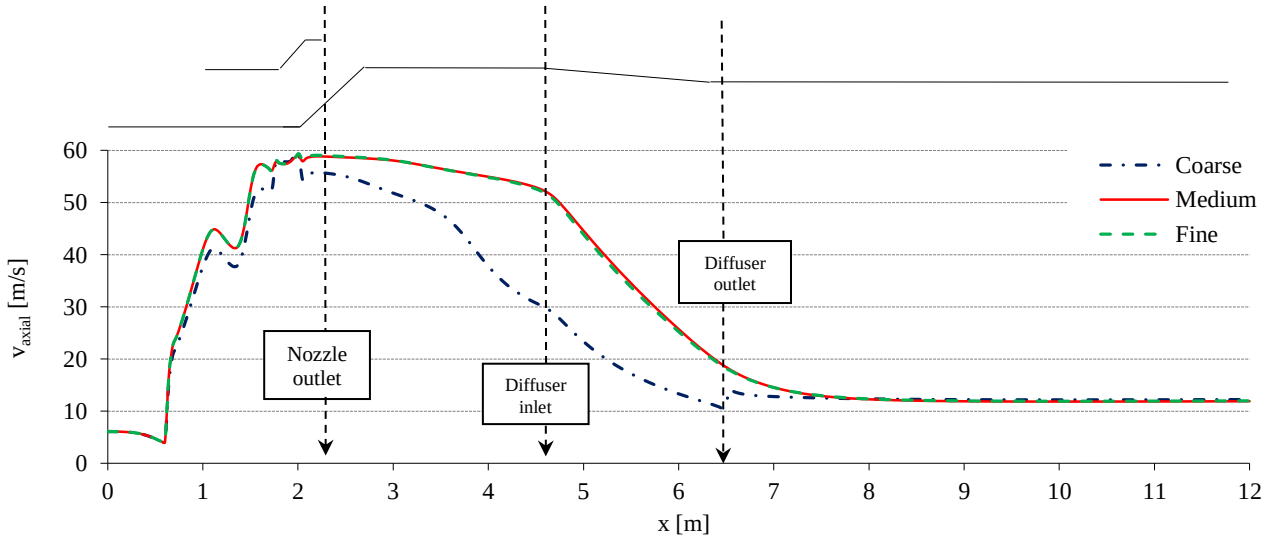

Figure 3 Grid independency

4.2. **Model validation**

4.2.1. *Convergence capabilities*

At first, we have noticed that the RSM can not reach a converged solution. Different techniques for the RSM model have been used: (i) lower accuracy first-order scheme for the convective terns, (ii) higher turbulence intensity at boundary condition and (iii) using a transient approach, instead of a steady state one. One reason could be that this model contains singularities that can cause divergence in regions of low turbulence. A second reason is that the equations are non-linear, and some of the non-linear forms are stiffer than other models. On the other hand, both the *k-ω* SST and the *k-ε* Realizable were able to reach the convergence. In particular, for the *k-ω* SST models, convergence was easily reached and a faster convergence was observed if compared to the *k-ε* Realizable. The *k-ε* Realizable were very sensible to the chosen turbulence boundary conditions. If the turbulence intensity boundary conditions were increased at the inlets, a more stable and faster simulation would result.

4.2.2. *Comparison with the experimental data*

The CFD model has been validated using pressure difference measurement between ejector outlet and secondary flow inlet $\Delta p_{experimental}$ = 480Pa. The *k-ε* Realizable and the *k-ω* SST numerical results were: $\Delta p_{k\text{-}\varepsilon,Realizable}$ = 550.3Pa and $\Delta p_{k\text{-}\omega,SST}$ = 478.3Pa. The *k-ω* SST provides a value closer to the measured data ($[\Delta p_{experimental} - \Delta p_{k\text{-}\omega,SST}]/\Delta p_{experimental}$ = -1.7%), while *k-ε* Realizable gives a slightly different result ($[\Delta p_{experimental} - \Delta p_{k\text{-}\varepsilon,Realizable}]/\Delta p_{experimental}$ = +16.7%). The reasons for the discrepancies will be explained in next section. It should not escape notice that the present validation concerns a global parameter and not local data. However, the correct evaluation of the pressure loss ensures that the mixing losses and friction losses are estimated correctly.

4.3. **Flow field investigation**

Once the CFD model has been validated, it can be used for investigating and understating the local flow behavior. Furthermore, this analysis can be used for understanding the reason why the *k-ε* Realizable experienced higher error if compared to the experimental measurements. After an insight of ejector flow field, the velocity and thermal field are investigated.

4.3.1. *Ejector flow field*

The flow inside the ejector can be classified into two regions: near field and far field. Very small time-scales are associated with region near nozzle exit where the jet has substantial gas dynamics concerning jet development. Larger time-scales and larger turbulent structures are associated with the low velocity in the downstream region. The present ejector has some peculiarity in the flow field. At first, near the secondary flow inlet there is a

sudden transition from square-sectioned duct to the suction chamber: this originates a recirculation which is captured by both the turbulence models (Figure 4, left). At second, there is flow separation in the primary flow curved duct (this issue is detailed in the next section). At last, at diffuser inlet (Figure 4, right), due to the adverse pressure gradient, the flow is separated and a recirculation bubble is generated (this issue is detailed in the next section).

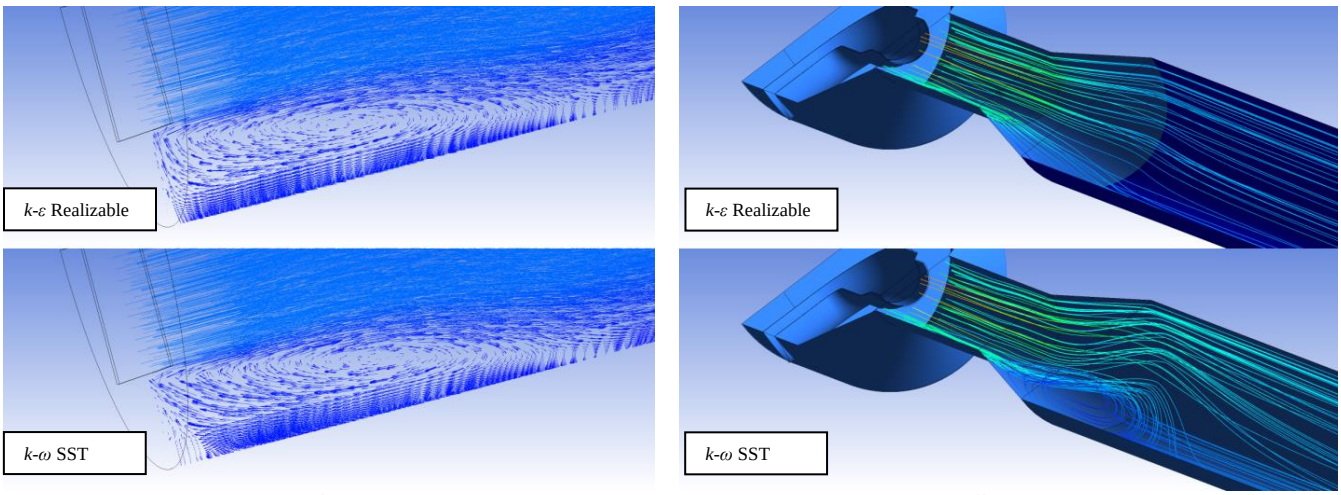

Secondary flow entrance *Diffuser inlet*

Figure 4 Flow recirculation

4.3.1. *Velocity field*

The velocity field is described using (i) the velocity profiles (Figure 5), (ii) the velocity contours (Figure 6) and (iii) the pathlines Figure 4, right): all these information are coupled for having the complete representation of the flow phenomena. We have considered the longitudinal (x-y plane) and the transversal (z-y plane) velocity profiles, which are represented in terms of a non-dimensional wall distances: $z^* = z/z_{wall}$ and $y^* = y/y_{wall}$.

The transversal profiles are symmetric and the maximum value is on the centerline (Figure 5a,b and Figure 6,up), as one could expect. Both the turbulence models provide similar results, except for the profile at nozzle distance equal to 6m. This correspond to the diffuser entrance, where the *k-ω* SST predict a flow recirculation. However, this flow behavior is better captured in the longitudinal velocity profiles. Another difference between the two models is the jet core length L_{jet} (which is evaluated on the x-y plane): it is slightly higher for the *k–ε* Realizable ($L_{jet,k\text{-}\varepsilon,Realizable} \approx 8.84 d_t$) if compared to the *k-ω* SST ($L_{jet,\ k\text{-}\omega,SST} \approx 6.11 d_t$), Where d_t is the diameter of the primary flow nozzle. This is due to the different modeling of the turbulent diffusion terms.

The longitudinal velocity profiles are non-symmetric (Figure 5c,d and Figure 6,bottom). Because of the 90° bend of the primary pipe, which originates a pressure gradients inside the primary flow pipe. Both the turbulence models predict the same flow separation in the curved pipe (Figure 6, bottom). The non-uniform pressure distribution at nozzle exit propagates along the mixing chamber and the diffuser, where the pressure increases: there is no choking phenomena in the present ejector and information can travel from upstream to downstream and vice-versa. Both the turbulence models predict similar flow behavior from primary nozzle exit to the diffuser inlet. This is shown both from velocity profiles (Figure 5c) and in velocity contours (Figure 6, bottom). The flow field prediction differs from diffuser inlet. Indeed, the *k-ω* SST capture a flow recirculation, while *k–ε* Realizable predicts a uniform pattern. This can be noticed by (i) velocity contour Figure 6, (ii) the pathlines Figure , right and (iii) the velocity distribution at x = 10 m (Figure 5d). The velocity profile predicted by the two turbulence models is very different: the *k–ε* Realizable predict an almost uniform velocity profile (the maximum difference from the mean value is about ± 18%) while, the *k-ω* SST predict a non uniform velocity profile (the maximum difference from the mean value is about ± 55%). These results are in agreement with the literature, where it is well known that flow separation at diffuser inlet occurs and that the *k-ω* SST is able to well predict the flow behavior in diffuser if compared to other turbulence models (with particular reference to the separation and reattachment points) [20]. The difference in the prediction of the pressure drop is due to the ability to predict the flow separation near diffuser inlet. A pressure drop is given by concentrated and distributed pressure drop. The *k-ω* SST predicts a higher concentrated pressure drop and a lower distributed pressure drop. Furthermore, the ejector length is considerable and the distributed pressure drop is predominant. This is the reason why $\Delta p_{k\text{-}\varepsilon,Realizable} > \Delta p_{k\text{-}\omega,SST}$.

4.3.1. *Temperature field*

The temperature field can be analyzed using the temperature profiles. In particular, Figures 5e,f compare the results of the two turbulence models. It is interesting to notice how the temperature profiles are comparable in the first part of the ejector (Figure 5e) and differs further downstream (Figure 5f), after the flow separation in the diffuser. These results are in accordance with the previous results: after the diffuser inlet the *k–ε* Realizable predict a more uniform velocity profile than the *k-ω* SST model because of the flow separation. At x = 10m, the thermal field is well developed and the difference between the centerline and wall value is 0.29 %. This suggests that the present ejector length is adequate for the thermal mixing and a shorter ejector could be used, thus reducing the pressure drop and the energy consumption at the fan. In the present simulations a constant Prandtl number is used. This may led to some errors in the prediction of the spread of passive scalar quantities (such as the temperature) [18].

Trasversal velocity profiles

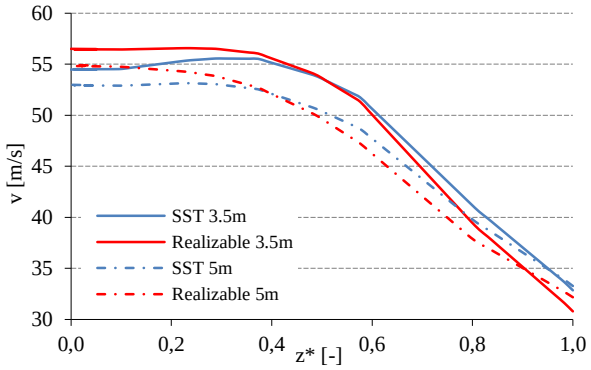

(a) Velocity transversal profile at 3.5 and 5 m

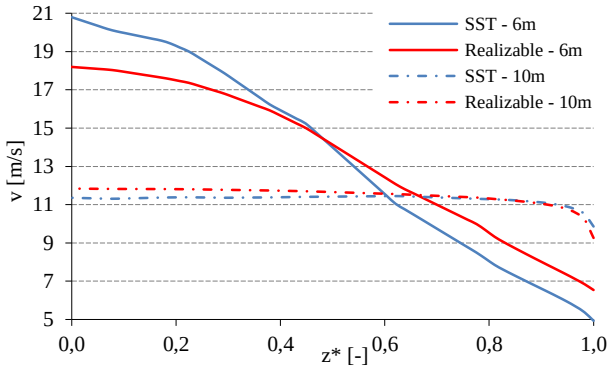

(b) Velocity transversal profile at 6m and 10m

Longitudinal velocity profiles

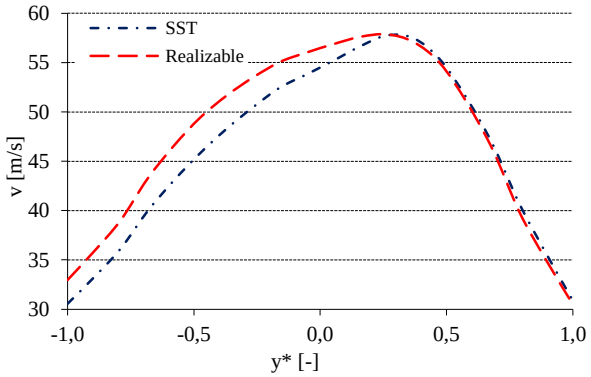

(c) Velocity longitudinal profile at 3.5m

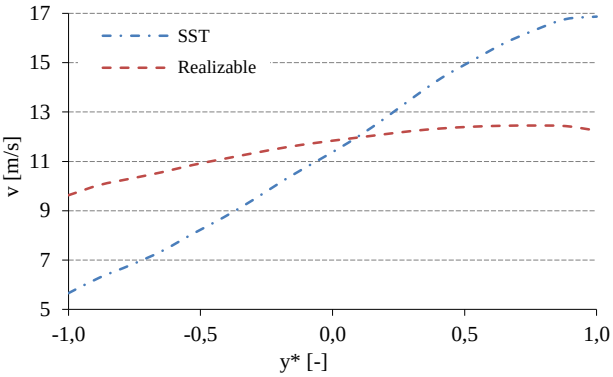

(d) Velocity longitudinal profile at 10m

Longitudinal temperature profiles

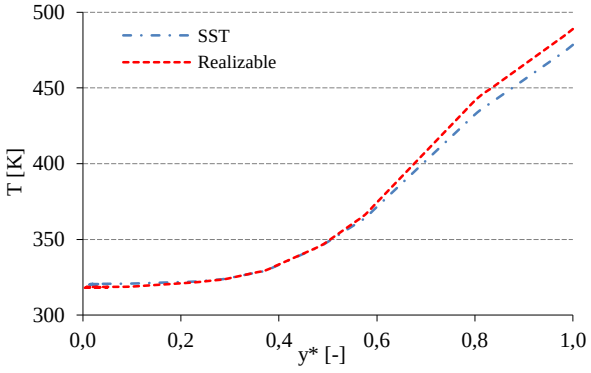

(e) Temperature longitudinal profile at 3.5m

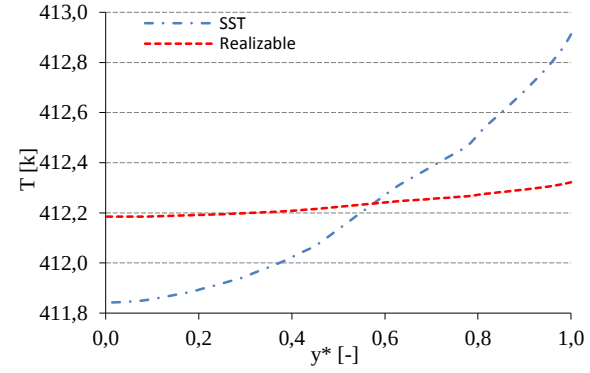

(f) Temperature longitudinal profile at 10m

Figure 5 Velocity and Temperature profiles

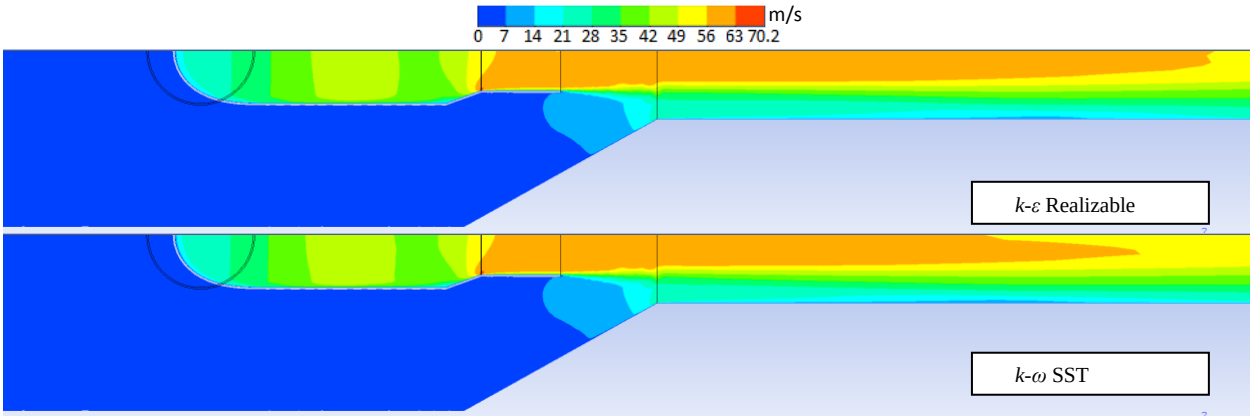

(a) Longitudinal velocity contour

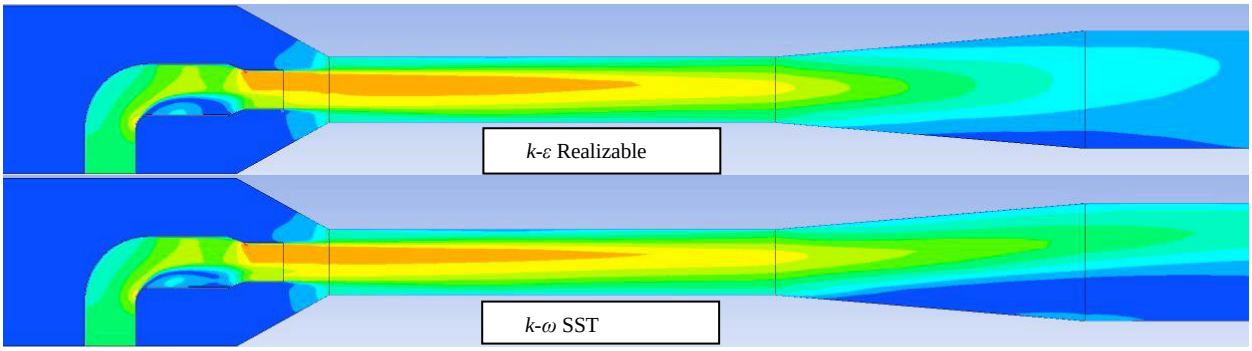

(b) Transversal velocity contour

Figure 6 Centerline velocity contours: (up) longitudinal and (bottom) transversal

5. Conclusions

In the revamping process of a galvanic plant furnace, in order to use low-grade energy sources, the whole system has to be updated. In the revamped plant, a convergent nozzle ejector is placed on the exhaust gases line. This paper studies the flow behavior of the ejector using a CFD analysis. The CFD analysis was needed because the models for convergent nozzle ejector are developed for PEM system. These systems are very different from the present case in terms of geometry, working fluids and operating conditions.

The CFD model was based on a 3D symmetric representation of the experimental ejector, using air and exhaust gases as working fluids. During the validation process of the CFD approach, different Reynolds-Averaged Navier–Stokes (RANS) turbulence model (RSM, k-ω SST and *k-ε* Realizable) are evaluated in terms of convergence capability and accuracy in predicting the pressure drop along the ejector: the k-ω SST performs better than *k-ε* Realizable, whereas RSM is unable to reach the convergence. The simulation results have been compared with pressure difference experimental data. The error between numerical results and experimental data are +16% and -1.7% for the *k-ε* Realizable and the *k-ω* SST model, respectably. The correct evaluation of the pressure loss ensures that the mixing losses and friction losses are estimated correctly. Those results have been explained and commented with considerations based on the local flow behavior and references to the literature. In particular, the *k-ω* SST was able to predict well the flow behavior in diffuser, with particular reference to the flow separation. The validation process ensures that the CFD results and the information obtained on the local flow phenomena (flow reparation, flow recirculation and adverse pressure gradient) were reliable.

Finally, suggestions for a future optimization of the system can be provided, based on the results. In the analyzed configuration, there are lots of flow separation, recirculation and irreversible phenomena: (i) flow recirculation at secondary flow inlet, (ii) flow separation for the primary flow and (iii) flow separation at diffuser inlet. All these phenomena create localized pressure drops. An optimized geometry, that would reduce those irreversibilities, would reduce the energy/exergy consumption. Furthermore, shorter ejector could be used for providing a similar thermal mixing, thus reducing the pressure drop and the energy consumption at the fan. Indeed, for entraining the same amount of secondary mass flow, the fan consumption would reduce. Further analysis are required to optimize the ejector geometry as well as to analyze a wider range of operating conditions.

Acknowledgments

The authors are deeply grateful to Dentella CHP, Combustion & Heat Processing for providing the experimental data and the information on the plant. The authors are also grateful to Matteo Carmelo Romano for the support.

References

[1] Y. Li, L. Zhu, Cost of energy saving and CO2 emissions reduction in China's iron and steel sector, Applied Energy, 130 (2014) 603-616.

[2] M. Arens, E. Worrell, Diffusion of energy efficient technologies in the German steel industry and their impact on energy consumption, Energy, 73 (2014) 968-977.

[3] E. Worrell, L. Price, N. Martin, Energy efficiency and carbon dioxide emissions reduction opportunities in the US iron and steel sector, Energy, 26 (2001) 513-536.

[4] S. He, Y. Li, R.Z. Wang, Progress of mathematical modeling on ejectors, Renewable and Sustainable Energy Reviews, 13 (2009) 1760–1780.

[5] L.G. Capitanio, CFD study of fluid dynamics of ejector and ducts in galvanizing plant, Master of Science Thesis, Politecnico di Milano, 2014.

[6] H.D. Kim, J.H. Lee, T. Setoguchi, S. Matsuo, Computational analysis of a variable ejector flow, Journal of Thermal Science, 15 (2006) 140-144.

[7] Y. Zhu, Y. Li, New teoretical model for convergent nozzle ejector in the proton exchange membrane fuell cell system, Journal of Power Sources, 191 (2009) 510-519.

[8] F. Kong, Y. Jin, T. Setoguchi, H. Kim, Numerical analysis of Chevron nozzle effects on performance of the supersonic ejector-diffuser system, Journal of Thermal Science, 22 (2013) 459-466.

[9] V. Dvorak, P. Safarik, Supersonic flow structure in the entrance part of a mixing chamber of 2D model ejector, Journal of Thermal Science, 12 (2003) 344-349.

[10] K. Pianthong, W. Seehanam, M. Behnia, T. Sriveerakul, S. Aphornratana, Investigation and improvement of ejector refrigeration system using computational fluid dynamics technique, Energy Conversion and Management, 48 (2007) 2556-2564.

[11] A. Hemidi, F. Henry, S. Leclaire, J.-M. Seynhaeve, Y. Bartosiewicz, CFD analysis of a supersonic air ejector. Part I: experimental validation of single-phase and two-phase operation, Applied Thermal Engineering, 29 (2009) 1523-1531.

[12] A. Hemidi, F. Henry, S. Leclaire, J.-M. Seynhaeve, Y. Bartosiewicz, CFD analysis of a supersonic air ejector. Part II: Relation between global operation and local flow features, Applied Thermal Engineering, 29 (2009) 2990-2998.

[13] J.H. Ferziger, M. Perić, Computational methods for fluid dynamics, Springer Berlin, 1996.

[14] Y. Bartosiewicz, Z. Aidoun, P. Desevaux, Y. Mercadier, CFD-experiments integration in the evaluation of six turbulence models for supersonic ejectors modeling, in: Proceedings of Integrating CFD and Experiments, Vol. 26, Glasgow, 2003, pp. 71-78.

[15] V. Dvorak, t. Vit, Experimental and numerical study of constant area mixing, in: 16th International Symposium on Transport Phenomena, Prague, 2006.

[16] J. Kolář, V. Dvořák, Verification of K-ω SST turbulence model for supersonic internal flows, World Academy of Science, Engineering and Technology, 81 (2011) 262-266.

[17] J. Gagan, K. Smierciew, D. Butrymowicz, J. Karwacki, Comparative study of turbulence models in application to gas ejectors, International Journal of Thermal Sciences, 78 (2014) 9-15.

[18] G. Besagni, R. Mereu, E. Colombo, CFD study of ejector efficiency, in: 12th Biennal Conference on Engineering systems Design and Analysis (ESDA2014), Copenaghen, Denmark, 2014.

[19] E. Colombo, F. Inzoli, R. Mereu, A methodology for qualifying industrial CFD: The Q3 approach and the role of a protocol, Computers & Fluids, 54 (2012) 56–66.

[20] S.M. El-Behery, M.H. Hamed, A comparative study of turbulence models performance for separating flow in a planar asymmetric diffuser, Computers & Fluids, 44 (2011) 248-257.